Coupling water fluxes with cell wall mechanics in a multicellular model of plant development

Ibrahim Cheddadi, Michel Génard, Nadia Bertin, Christophe Godin

Coupling water fluxes with cell wall mechanics in a multicellular model of plant development

Ibrahim Cheddadi[a,b,1], **Michel Génard**[c], **Nadia Bertin**[c], **and Christophe Godin**[b,d,1]

[a]Univ. Grenoble Alpes, CNRS, Grenoble INP, TIMC-IMAG, 38000 Grenoble, France; [b]Virtual Plants, Inria, Montpellier, France; [c]PSH, INRA, Avignon, France; [d]Laboratoire Reproduction et Développement des Plantes, Univ Lyon, ENS de Lyon, UCB Lyon 1, CNRS, INRA, Inria, F-69342, Lyon, France

This manuscript was compiled on January 8, 2019

The growth of plant organs is a complex process powered by osmosis that attracts water inside the cells; this influx induces simultaneously an elastic extension of the walls and pressure in the cells, called turgor pressure; above a threshold, the walls yield and the cells grow. Based on Lockhart's seminal work, various models of plant morphogenesis have been proposed, either for single cells, or focusing on the wall mechanical properties. However, the synergistic coupling of fluxes and wall mechanics has not yet been fully addressed in a multicellular model. This work lays the foundations of such a model, by simplifying as much as possible each process and putting emphasis on the coupling itself. Its emergent properties are rich and can help to understand plant morphogenesis. In particular, we show that the model can display a new type of lateral inhibitory mechanism that could contribute to the amplification of growth heterogeneities, essential for shape differentiation.

Plant growth and morphogenesis | Biophysics | Mathematical modelling | Emergence | Lateral inhibition

Plants grow throughout their lifetime at the level of small regions containing undifferentiated cells, the meristems, located at the extremities of their axes. Growth is powered by osmosis that tends to attract water inside the cells. The corresponding increase in volume leads to simultaneous tension in the walls and hydrostatic pressure (so-called turgor pressure) in the cells. Continuous growth occurs thanks to the yielding of the walls to these stretching forces [1–3].

This interplay between growth, water fluxes, wall stress and turgor was first modelled by Lockhart in 1965 [4], in the context of a single elongating cell. Recent models focused on how genes regulate growth at more integrated levels [5–9]. To accompany genetic, molecular, and biophysical analyses of growing tissues, various extensions of Lockhart's model to multicellular tissues have been developed. The resulting models are intrinsically complex as they represent collections from tens to thousands of cells in 2- or 3-dimensions interacting with each other. To cut down the complexity, several approaches abstract organ multicellular structures as polygonal networks of 1D visco-elastic springs either in 2D [7, 10–12] or in 3D [6, 13] submitted to a steady turgor pressure. Other approaches try to represent more realistically the structure of the plant walls by 2D deformable wall elements able to respond locally to turgor pressure by anisotropic growth [8, 14, 15].

Most of these approaches consider turgor as a constant driving force for growth, explicitely or implicitly assuming that fluxes occur much faster than wall synthesis. Cells then regulate the tissue deformations by locally modulating the material structure of their walls (stiffness and anisotropy) [6, 16–20]. However, the situation in real plants is more complex: turgor heterogeneity has been observed at cellular level [21, 22], which challenges the assumption of very fast fluxes. As a matter of fact, the relative importance of fluxes or wall mechanics as limiting factors to growth has fuelled a long standing debate [3, 23] and is still an open question. Moreover, from a physical point of view, pressure is a dynamic quantity that permanently adjusts to both mechanical and hydraulic constraints, which implies that a consistent representation of turgor requires to model both wall mechanics and hydraulic fluxes.

The aim of this article is to explore the potential effect of coupling mechanical and hydraulic processes on the properties of the "living material" that corresponds to multicellular populations of plant cells. To this end, we build a model that describes in a simple manner wall mechanics and cell structure, but do not compromise on the inherent complexity of considering a collection of deformable object hydraulically and mechanically connected.

The article is organized as follows (see Fig. 1): we first recall the Lockhart-Ortega model and its main properties. Then we explore two simple extensions of this model: first we relax the constraint of uniaxial growth in the case of a single polygonal cell; then we study how two cells hydraulically connected interact with each other. Finally we describe our multicellular and multidimensional model and numerically explore its properties.

Significance Statement

Plant cells are surrounded by a rigid wall that prevents cell displacements and rearrangements as in animal tissues. Therefore, plant morphogenesis relies only on cell divisions, shape changes, and local modulation of growth rate. It has long been recognized that cell growth relies on the competition between osmosis that tends to attract water into the cells and wall mechanics that resists to it, but this interplay has never been fully explored in a multicellular model. The goal of this work is to analyze the theoretical consequences of this coupling. We show that the emergent behavior is rich and complex: among other findings, pressure and growth rate heterogeneities are predicted without any ad-hoc assumption; furthermore the model can display a new type of lateral inhibition based on fluxes that could complement and strengthen the efficiency of already known mechanisms.

This study was initiated by C.G., M.G., and N.B. I.C. designed the model with the help of C.G. and M.G, performed the mathematical calculations with the help of C.G., designed the resolution algorithm, implemented it, ran simulations, and explored the parameters space. I.C. and C.G. analyzed the results and wrote the manuscript with inputs from other authors.

The authors declare no conflict of interest.

[1]To whom correspondence should be addressed. E-mail: ibrahim.cheddadi@univ-grenoble-alpes.fr, christophe.godin@inria.fr

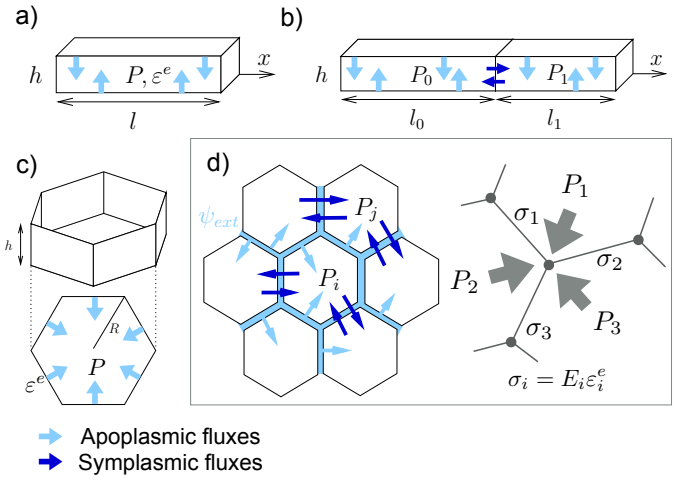

Fig. 1. Hierarchy of models presented in this article. Main variables are turgor P and elastic deformation ε^e. **a**) Lockhart-Ortega model: uniaxial growth in the x direction of a cylindrical cell of length l; the section perpendicular to x is a square of side h. **b**) two cells extension, both growing along x; **c**) 2D extension of a single cell growth; **d**) Multicellular, multidimensional model; left: fluxes, right: mechanical equilibrium; the stress σ is proportionnal to the elastic deformation ε^e; E is the elastic modulus.

The Lockhart model

In 1965, Lockhart [4] derived the elongation of a cylindrical plant cell by coupling osmosis-based fluxes and visco-plastic wall mechanics. Ortega [24] extended this seminal model to include the elastics properties of the cell walls. We recall here the main properties of this model, see Fig. 1a for the geometrical configuration.

Cell wall elongation. It is expressed as a rheological law [4, 24]: the total strain rate of the walls $\dot{\varepsilon}$ is decomposed into the sum of a plastic and an elastic strain rate:

$$\dot{\varepsilon} = \phi^w (P - P^Y)_+ + \frac{1}{\bar{E}} \frac{\mathrm{d}P}{\mathrm{d}t}, \qquad [1]$$

where the extensibility ϕ^w (inverse of a viscosity) describes the ability of the cell to synthesize wall material, and $\bar{E}$ is an effective elastic modulus. Here, ϕ^w and $\bar{E}$ both depend on cell wall thickness. The notation $(x)_+$ denotes x if $x > 0$ and 0 otherwise for any real number x.

Water uptake. Lockhart described water uptake by the cell as a flux through a semi-permeable membrane characterized by its surface A and its permeability L^a. Assuming the membrane is perfectly impermeable to solutes, the rate of volume change is the result of a difference between the water potential Ψ of the cell and Ψ_{ext} of its exterior [25]:

$$\frac{\mathrm{d}V}{\mathrm{d}t} = AL^a \left(\Psi_{ext} - \Psi\right), \qquad [2]$$

The cell water potential $\Psi = P - \pi$ results from the antagonistic effect of the cell hydrostatic pressure P that tends to expel water from the cell and its osmotic pressure π that tends to attract water inside the cell. In the case of a single solute of concentration c, we have $\pi = RTc$ where R is the ideal gas constant and T the temperature. Let us denote $\phi^a = \frac{AL^a}{V}$ which has the same dimension as ϕ^w. Assuming that the fluxes occur mostly on the lateral surface, the ratio A/V is constant in the configuration of a cylindrical cell. After division by V, Eq. (2) turns into:

$$\dot{\gamma} = \phi^a \left(P^M - P\right). \qquad [3]$$

where $P^M = \Psi_{ext} + \pi$ quantifies the power of the osmotic pump: it is positive if π is high enough to overcome the negative water potential of the exterior of the cell. Growth ($\dot{\gamma} > 0$) implies $P < P^M$ and hence P^M is an upper bound for turgor, above which the cell would lose water to the exterior. The additional condition for growth $P > P^Y$ (see above) requires $P^M > P^Y$: growth is possible only when the osmotic pump is able to overcome the mechanical resistance of the walls.

In order to keep the analysis as simple as possible, we take here and in the remaining of the article P^M constant with time and homogeneous among the cells, which corresponds for instance to constant π and Ψ_{ext}. This choice will be commented in the discussion section.

Coupling hydraulics and mechanics for a single cell. Equating the expressions of strain rate $\dot{\varepsilon}$ from Eq. (1) and relative growth rate $\dot{\gamma}$ from Eq. (3) ensures that the requirements for water uptake and yield of the cell wall are simultaneously satisfied. This means that turgor P, that is present in both equations, has to be adjusted to satisfy both hydraulic and mechanical constraints. The resolution of the model is detailed in Supplementary Information (SI), Eqs. (S3)-(S4). The time dependent solutions can be analytically determined and we find that P and $\dot{\gamma}$ converge towards a stationary solution $(P^*, \dot{\gamma}^*)$: first, P^* writes

$$P^* = \alpha^a P^M + (1 - \alpha^a) P^Y, \qquad [4]$$

where

$$\alpha^a = \frac{\phi^a}{\phi^a + \phi^w} \in [0, 1] \qquad [5]$$

measures the relative importance of ϕ^a compared to ϕ^w. In the limit $\phi^a \ll \phi^w$ ($\alpha^a = 0$), any excess of turgor above the threshold is relaxed by cell wall synthesis and turgor is minimal at $P = P^Y$. Conversely, in the limit $\phi^w \ll \phi^a$ ($\alpha^a = 1$), the wall synthesis is not able to relax turgor, which reaches then its maximal value $P = P^M$. Second, the expression of the relative growth rate is:

$$\dot{\gamma}^* = \frac{\phi^a \phi^w}{\phi^a + \phi^w} (P^M - P^Y), \qquad [6]$$

or equivalently: $P^M - P^Y = \left(\frac{1}{\phi^a} + \frac{1}{\phi^w}\right) \dot{\gamma}^*$. This equation is the analog of Ohm's law $\Delta U = (R_1 + R_2) I$ with two resistors $R_1 = 1/\phi^a$ and $R_2 = 1/\phi^w$ in series: growth can be limited by either hydraulic conductivity or wall synthesis.

Link with wall rheology. Wall expansion law (Eq. (1)) can be equivalently described as a function of wall stress σ rather than cell turgor P: in the cylindrical geometry of the Lockhart-Ortega model, we find (see SI for the calculations) $P = 2\frac{w}{h}\sigma$, where w is the width of the walls and h their height. Thanks to this relation, Eq. (1) translates into $\dot{\varepsilon} = \frac{1}{E}\frac{\mathrm{d}\sigma}{\mathrm{d}t} + \Phi^w(\sigma - \sigma^Y)_+$, where $E = \frac{h}{2w}\bar{E}$ (resp. $\Phi^w = \frac{2w}{h}\phi^w$) is the intrinsic elastic modulus (resp. extensibility) of the walls. Let $\varepsilon^e = \sigma/E$ be the so-called elastic deformation of the walls. It is dimensionless and can be measured from the image analysis

of experiments, without the knowledge of the elastic modulus. The wall rheology is then described as follows:

$$\dot{\varepsilon} = \frac{\mathrm{d}\varepsilon^e}{\mathrm{d}t} + \Phi^w E(\varepsilon^e - \varepsilon^Y)_+, \qquad [7]$$

where $\varepsilon^Y = \sigma^Y/E$ is the threshold elastic deformation. Note that $\frac{1}{\Phi^w E}$ can be interpreted as the characteristic time of wall synthesis.

Multidimensional and multicellular models

A multicellular extension of the Lockhart-Ortega model adapted to the study of morphogenesis requires first to relax the constraint of uniaxial growth and allow multidimensional geometries, and second is complexified by the possibility of fluxes between cells. We study separately the effect of each of these extensions before presenting the complete model.

First extension: Multidimensional growth. In order to keep the analysis as simple as possible, we study here the expansion of a single 2D cell whose shape is a regular polygon with n edges (see Fig. 1c). This model allows to evaluate the effect of a varying surface/volume ratio compared to the Lockhart-Ortega model where this ratio is constant. The fluxes are described in the same way as for Lockhart's model (Eq. (2)) but wall synthesis is described with Eq. (7), as a function of elastic deformation instead of turgor. We find (see SI for detailed calculations) that the relation between cell turgor and wall stress becomes $P = \frac{w}{R\cos(\pi/n)}\sigma$ where R is the cell radius. In contrast with the Lockhart-Ortega model, the ratio P/σ is no more constant as cell grows, and the turgor vanishes at long times if the stress remains in the order of magnitude of the threshold. Note also that for a given stress the turgor decreases with the number of edges n. Therefore, the yield turgor P^Y depends both on n and R and is not a well defined parameter. It suggests also that cells with less neighbours should have a higher turgor, as experimentally observed in [21, 22].

The prediction of growth rate requires a numerical resolution of the model (see SI). The parameters are chosen to ensure a turgor of the order of 0.5 MPa and a relative growth rate of the order of 2% per hour, using the predictions Eq. (4) and Eq. (6). First let's examine the case of a cell of initial radius $R = 10\mu$m for which wall synthesis is the limiting factor to growth (case $\alpha^a = 0.9$ in SI, fig. S2). We find that it results initially in an accelerating growth (the bigger the cell, the faster the growth), much faster than predicted by the Lockhart model, during which the elastic deformation of the walls can reach values up to 20%. The ratio area/surface $= 1/R$ decreases with growth and there is less and less water available compared to the volume; as a consequence, the relative growth rate vanishes at long times after this initial accelerating phase.

In the case where the fluxes are already limiting in the initial state (case $\alpha^a = 0.1$ in SI, Fig. S2), the initial behaviour is closer to the predictions of the Lockhart model but the relative growth rate still vanishes at long times.

Altogether, these results show that a non constant surface/volume ratio deeply modifies the behavior of the model compared to the Lockhart model. In particular, flux and wall synthesis as limiting factors fro growth are no more equivalent.

Second extension: Multicellular growth. Then, we study a simple multicellular extension of the Lockhart-Ortega model where two cylindrical cells $i = 0, 1$ are in contact through one of their wall (see Fig. 1b). The cells can absorb water from their lateral surface and in the meantime exchange water with each other through their common wall. We look for stationary solutions: $\frac{\mathrm{d}P_i}{\mathrm{d}t} = 0$ and $\frac{1}{V_i}\frac{\mathrm{d}V_i}{\mathrm{d}t} = \mathrm{Cst}$.

We set for both cells a common value of P^M, L^a and ϕ^w, while the value of the yield turgors P_i^Y can differ; this corresponds for instance to a heterogeneity of wall elastic modulus or yield deformation. For the sake of convenience, we refer to fluxes between cells as symplasmic fluxes, characterized by a water conductivity L^s, and to fluxes from the water source as apoplasmic fluxes, characterized by a water conductivity L^a. Assuming that the symplasmic fluxes occur through plasmodesmata that are permeable to both water and solutes, the flux equation writes

$$\frac{\mathrm{d}V_i}{\mathrm{d}t} = A_i L_i^a (P^M - P_i) + A_{01} L^s (P_j - P_i),$$

where $j = 1 - i$, and A_{01} is the surface of the common wall of cells 0 and 1. We introduce the number $\phi^s = 2A_{01}L^s/V_i$ which has the same dimension as ϕ^a and ϕ^w. In order to allow an analytical resolution of this set of equations, we assume ϕ^s to be constant with time, and consider it in this section as a parameter of the model. Thus, we have

$$\dot{\gamma}_i = \phi^a \left(P^M - P_i\right) + \frac{\phi^s}{2}(P_j - P_i). \qquad [8]$$

We introduce the dimensionless number

$$\alpha^s = \frac{\phi^s}{\phi^s + \phi^a} \in [0, 1]$$

which represents the relative importance of symplastic fluxes with respect to apoplastic ones. We combine this flux equation with the growth equation Eq. (1) and find analytical solutions for any values of the parameters (see SI). We use here the following set of control parameters:

$$P^M, P_i^Y, \dot{\gamma}_0^*, \alpha^a, \alpha^s,$$

and fix the value $\dot{\gamma}_0^* = 2\% \cdot \mathrm{h}^{-1}$; this way, the parameters space to explore is reduced to $(P^M, P^Y, \alpha^a, \alpha^s)$. When $\alpha^s = 0$, the cells are completely isolated one from another and reach turgors P_i^* and growth rates $\dot{\gamma}_i^*$ as predicted by the Lockhart model (Eq. (4) and Eq. (6)). In particular, the condition $P^M > P_i^Y$ ensures that each cell is growing. When $\alpha^s > 0$, the fluxes between cells modify this behaviour. We restrict to the case $P_0^Y < P_1^Y < P^M$, which corresponds to less mechanical constraints on cell 0 than cell 1; therefore we can expect $P_1 > P_0$ and $\dot{\gamma}_1 < \dot{\gamma}_0$. The calculations show a complex non linear behaviour that is illustrated in Fig. 2, in which the parameters subspace (α^a, α^s) is explored for given values of P_i^Y and P^M (detailed calculations are provided in SI). Let $\Delta P^Y = P_1^Y - P_0^Y > 0$ be the difference of the two yield turgors and $\bar{P}^Y = 0.5(P_0^Y + P_1^Y)$ their average; we also introduce the dimensionless number

$$\rho = \frac{\Delta P^Y}{2(P^M - \bar{P}^Y)}. \qquad [9]$$

Note that the hypothesis $P_0^Y < P_1^Y < P^M$ is equivalent to $\rho \in]0, 1[$.

We find that the subspace (α^a, α^s) can be divided in two main regions separated by the curve $\alpha^s = \frac{1-\rho}{1-\alpha^a}$ (see Fig. 2a):

surprisingly, in the region $\alpha^s > \frac{1-\rho}{1-\alpha^a}$, only cell 0 is growing ($\dot{\gamma}_0 > 0$, $\dot{\gamma}_1 = 0$, and equivalently $P_0 > P_0^Y$, $P_1 < P_1^Y$). Hence, the growth of cell 1 is inhibited by fluxes with cell 0. Conversely, in the region $\alpha^s < \frac{1-\rho}{1-\alpha^a}$ both cells are growing ($\dot{\gamma}_i > 0$ and equivalently $P_i > P_i^Y$). The size of the region $\alpha^s > \frac{1-\rho}{1-\alpha^a}$ increases with ρ and fills the whole square $[0,1] \times [0,1]$ when $\rho \to 1$; such values can be reached when ΔP^Y is large and / or P^M is close to $\bar{P}^Y$.

More quantitatively, Figs. 2d-e) show that $\dot{\gamma}_1$ is always below $\dot{\gamma}_1^*$, while $\dot{\gamma}_0$ is always above $\dot{\gamma}_0^*$ and can reach up to twice this value. Furthermore, maximal values of $\dot{\gamma}_0$ coincide with minimal values of $\dot{\gamma}_1$: this confirms quantitatively that the growth of the cell with less favorable mechanical condition is slowed down if not inhibited by the growth of its neighbour. This shows also that the growth rate heterogeneity is amplified by fluxes.

Turgor heterogeneity is also affected by fluxes (see Figs. 2b-c): when α^s is close to zero, the cells are hydraulically isolated and their turgors vary with α^a as predicted by Lockhart model (Eq. (4)), this is where the turgor heterogeneity is maximal. Conversely, when α^s is close to 1, there is no hydraulic resistance between the two cells and the two turgors are equal. Between these two limits, P_0 is only slightly affected and remains in the $[P_0^Y, P^M]$ interval; conversely, P_1 is dramatically affected as it shifts from the interval $[P_1^Y, P^M]$ when $\alpha^s = 0$ to the interval $[P_0^Y, P^M]$ when $\alpha^s = 1$. Therefore, as $P_0^Y < P_1^Y$, there is a region where $P_1 < P_1^Y$ which corresponds to the region $\alpha^s > \frac{1-\rho}{1-\alpha^a}$, where cell 1 is not growing.

Finally, we have seen that intercellular fluxes tend to increase (resp. decrease) growth rate (resp. turgor) heterogeneities; the cell with less mechanical constraints takes control over the other one and imposes its turgor, which can lead the other one to stop growing. The growing cell then benefits from the water resources of the other cell and its growth is all the more increased.

Generalization: a multidimensional and multicellular model of growth. We consider (see Fig. 1d) a collection of N cells that form a (non necessarily regular) 2D mesh with a fixed topology (distribution of neighbours) as is the case with plant tissues when no division occurs.

The cell walls rheology is described by the visco-elasto-plastic law (Eq. (7)) of the Ortega model and the fluxes toward a cell i are described as in the simple multicellular model presented above:

$$\frac{\mathrm{d}V_i}{\mathrm{d}t} = A_i L_i^a (P^M - P_i) + \sum_{j \in n(i)} A_{ij} L_{ij}^s \left(P_j - P_i\right), \qquad [10]$$

where $n(i)$ is the set of neighbours of cell i, A_{ij} is the area of the common wall with cell j, L_{ij}^s its permeability (it is symmetric: $L_{ij}^s = L_{ji}^s$), and L_i^a is the permeability of the lateral walls to the supply of water.

The last missing part to obtain a closed set of equation is the mechanical equilibrium, that allows to link cells turgors, walls tensions, and geometry. Contrary to the cases studied above, no explicit expression of turgors as a function of stresses can be obtained and the equilibrium has to be solved at each time step. Let P_i be the turgor pressure in each cell i. The tissue being at every moment in a quasi-static equilibrium, pressure forces on wall edges and elastic forces within walls balance exactly at each vertex v:

$$\frac{1}{2} \sum_{k \in f(v)} \Delta_k P \; S_k \boldsymbol{n}_k + \sum_{k \in f(v)} E_k \varepsilon_k^e s_k \boldsymbol{e}_{k,v} = 0, \qquad [11]$$

where $f(v)$ is the set of faces adjacent to junction v, $\Delta_k P = P_{k_1} - P_{k_2}$ is the pressure jump across face k, with $k_1 < k_2$ being indices of the cells across face k, $S_k = h l_k$ is the area of the face k on which pressure is exerted, $\boldsymbol{n}_k$ is the normal vector to face k, oriented from cell k_1 to cell k_2, and $s_k = hw$ is the cross-section area of the face, on which the elastic stress is exerted; finally, $\boldsymbol{e}_{k,v}$ is the unit vector in the direction of face k, oriented from junction v to the other end of face k.

Coupling mechanical and hydraulic models. In the Lockhart-Ortega model, the compatibility between wall enlargement and cell volume variation is automatically enforced through the geometrical constraint of uni-directional growth that leads to the identity between the relative growth rate of the cell and the strain rate of the walls. In contrast, in the multicellular model, this identity is no longer true. One has to solve the closed set of equations Eq. (7)-Eq. (10)-Eq. (11) with respect to the unknowns X, P, and ε^e.

Despite its apparent simplicity, the problem to be solved is not straightforward as water fluxes induce potentially long range interactions. In this respect, it differs from most vertex-based models (*e.g* [11, 26]) where turgor is an input of the model. The numerical resolution required the development of an original algorithm (see SI) implemented in an in-house code.

Numerical experiments: growth of primordia in the shoot apical meristem (SAM). The properties of this model cannot be as thoroughly studied as those of the simpler models presented above, first because of the numerical cost of the resolution, but above all because it allows an infinite variety of geometries and spatial distribution of its parameters. We present here a numerical experiment that illustrates on the one hand how the properties of the simple multidimensional and multicellular submodels are combined in the generalized model; in turn the study of these models helps us to anticipate the properties of the generalized model. And on the other hand, we show that this model is readily applicable to the study of systems of biological interest.

Growth heterogeneities can be triggered by the local modulation of the mechanical properties of the cell walls [27]. In SAMs, new organs are initiated by a local increase in growth rate that leads to the appearance of small bumps. Measurements show that physico-chemical properties of walls are modified so that mechanical anisotropy and elastic modulus are decreased. In our 2D model, we can explore what effect a local softening of the walls has on growth rate and turgor heterogeneities; based on our previous analysis of the model in simple configurations, we expect that the growth heterogeneities will be maximal for parameters such that the growth is restricted by fluxes rather than wall synthesis (low α^a), cell-cell conductivity is large, and the walls deformations are just above the growth threshold, which can be enforced by a low value of the osmotic pressure (yet large enough to ensure growth). The set of parameters (REF) is chosen according to these criteria; then we explore the effect of a higher α^a ((ALPHA+) set) and lower cell-cell conductivity ((CC-) set)

that should both decrease the growth heterogeneities, and also test the effect of a lower osmotic pressure ((PM-) set) that should conversely increase the growth heterogeneity. See table 1 in SI for the values of the parameters corresponding to these sets and SI for more precise explanations.

We build a mesh made primarily of hexagons (see Fig. 3a) and first let it grow with homogeneous parameters until the elastic regime ends and plastic growth occurs. Then we divide by two the elastic modulus of a small group of cells (marked with a white star in Fig. 3a) that will be referred to as "bump cells" thereafter. All the details of the computations are presented in SI. First, Fig. 3b shows that the multicellular system grows globally in the same way as the single hexagonal cell studied above; it diverges from the Lockhart predictions because the ratio A/V of the cells is not constant: the (ALPHA+) simulations exhibit a very large initial growth rate that decreases only when the cells are so large that water fluxes become limiting. The (PM-) set leads to a roughly twice lower growth rate than (REF). The set (CC-) leads to the same dynamics at the tissue level as (REF), because the total influx of water is not affected by fluxes between cells in this setup.

Then we turn to the observation of heterogeneities: we focus on the differences between the bump region and the rest of the tissue. For all the parameters sets, Fig. 3c shows that turgor is in general lower in bump cells, but the gap varies depending on the parameters, as it has been predicted by the study of the two-cells model: compared to (REF), the heterogeneity in turgor is increased by a lower cell-cell conductivity (set CC-), and decreased by a larger value of α^a (set ALPHA+). Decreasing the value of P^M (set PM-) does not alter much the turgor heterogeneity compared to (REF). The maps of turgor (Figs. 3e,g,i,k) confirm visually these observations.

Fig. 3d shows the time evolution of $\dot{\gamma}/\dot{\gamma}^*$ where $\dot{\gamma}^*$ is the relative growth rate predicted by the Lockhart model (see Eq. (6)); its value is 2% h^{-1} for (REF), (CC-) and (ALPHA+), and 0.5% h^{-1} for (PM-). In the considered time frame, the relative growth rate of bump cells is always higher except for (ALPHA+): after an initial fast increase where bump cells grow faster, the tendency is inversed at $t \approx 20$h because the bump cells have grown so much that fluxes become limiting. In the (REF) simulation, while the growth rate of non bump cells is almost constant and close to $\dot{\gamma}^*$, the growth rate of the bump cells is up to 6 times $\dot{\gamma}^*$ at the beginning of the simulation and progressively decreases toward $\dot{\gamma}^*$. As a result of this large discrepancy, the bump region can be clearly distinguished from the rest of the tissue (Figs. 3e-f). In (CC-), the growth rate of the non bump cells is close to that of (REF), but the growth rate of the bump cells is much lower (Fig. 3d). As a result, the global shape remains convex and the bump is not clearly detached from the rest of the tissue (Figs. 3i-j). Note that (CC-) corresponds to a lower value of α^s compared to (REF), which corresponded to a lower growth heterogeneity with the two-cells model studied above; this is also confirmed by the lower cell-cell fluxes towards the bump cells for (CC-), see the arrows in Figs. 3e,i. The (ALPHA+) simulation exhibits also a convex shape (Fig. 3k-l); it corresponds to a larger value of α^a than (REF), and similarly to the two-cells model studied above, the growth rate heterogeneity is lower than (REF). Finally, the set (PM-) corresponds to an increase of the dimensionless parameter ρ (see Eq. (9)), and accordingly to an increase in growth rate heterogeneity as can be seen with Fig. 3d. Consequently, the bump region can clearly distinguished from the rest of the tissue, even better than (REF) (Fig. 3g-h); moreover, the growth of the cells close to the bump seems to be inhibited by fluxes as explained in the two-cells model described above and further explored below.

Flux-based lateral inhibition predicted by the model. As we saw, cells that benefit from better mechanical conditions for growth (in the present case a lower elastic modulus) have a lower turgor than the other cells, and therefore attract water from them. Not only does it amplify their growth but it also inhibits the growth of their neighbours. Such a lateral inhibition mechanism is important for morphogenesis, as it allows very large growth rate heterogeneities and the appearance of well differentiated shapes (in the present case the appearance of a bump on the surface of the meristem). The efficiency of this mechanism varies depending on the position in the parameters space: for instance it is increased if the cell-cell conductivity L^s (or equivalently α^s) is increased (see Fig. 4a-d); even the whole tissue can be inhibited. Inhibited cells can also relax the tension of their walls and decrease their volume (see Fig. 4a). To further explore and quantify the spatial range of this inhibition process, we extended our two-cells model (see SI for detailed equations) to a chain of $2N+1$ cells where the central cell has twice softer walls. We numerically solved the corresponding system of differential equations for the set (REF) and then for a large range of values of L^s. Fig. 4e shows that the number $2N_i$ of inhibited cells scales with $\sqrt{L^s}$. We computed the prefactor c (such that $N_i \approx c\sqrt{L^s}$) for values of $(\alpha^a, P^M) \in [0.05, 0.35] \times [0.51, 0.85]$ (the interval for P^M is in MPa) and plotted its value in the (α^a, P^M) space (Fig. 4f). This shows that the inhibition is favored by low values of α^a and $P^M - P^Y$.

Discussion

A minimal model with a complex and rich behavior. The model proposed in this article is a minimal multicellular and multidimensional extension of the Lockhart 1-D single cell model; it can be regarded as a conceptual tool to study the interplay between fluxes and wall mechanics in a multicellular tissue. Wall expansion is modeled with a visco-elasto-plastic rheological law, while fluxes derive from water potential gradients. These two contributions are integrated into the mechanical equilibrium and interact through the pressure term. Contrary to most previous approaches, turgor is not an input of the model but a variable that adjusts simultaneously to mechanical, hydraulic, and geometrical constraints. First of all, this leads to a physically consistent representation of turgor: for instance, the model predicts that cells with softer walls have a lower turgor. Moreover, this has deep implications at tissue level: in the previous example, lower turgor is associated with a faster growth which can be itself amplified by fluxes that follow decreasing pressure gradients.

Thanks to the simplicity of the model, the predicted behavior can be analyzed and interpreted with two submodels built from the Lockhart model: first, a 1-D multicellular submodel was build with two or more side-by-side cells; it was used to study the growth of competing cells with heterogeneous properties. Key ingredients here are the wall synthesis threshold, the fact that fluxes and growth can relax turgor, and cell to cell fluxes that allow long range interactions. Second, in a

1-D system, cells are considered essentially as cylinders and their surface-to-volume ratio is constant. We thus extended also the Lockhart model in two dimensions, where cells have more degree of freedom to change their shape. In particular their allometric surface-to-volume ratio may then vary. This new possibility induces additional complexity in the tissue development as the rate of growth of cell surfaces may become a limiting factor for growing cells.

A potentially new type of lateral inhibition mechanism. Depending on mechanical and hydraulic parameters of tissue regions, the model exhibits different growth regimes corresponding to either uniform or differential growth. One unexpected consequence of such an hydraulic-mechanical coupling at the tissue level is the observation that in certain regions of the parameter space where cell-to-cell hydraulic exchanges are non-limiting, growing tissue may exert an inhibiting influence on the growth of neighboring regions. This may be interpreted as a lateral inhibition mechanism. It has for long been recognized that lateral inhibitory mechanisms play a key role in setting some morphogenetic patterns in procaryotes (e.g. [28]), animals (e.g. [29, 30]) or plants (e.g. [31, 32]). Lateral inhibition operates in these systems via chemical signals, such as delta-notch in animals or auxin in plants. Our model predicts the existence of a novel type of lateral inhibition mechanism based on the coupling between mechanics and water fluxes. Previous observations of tissue growth suggest that such a phenomenon may occur in real tissues. In the shoot apical meristem for instance, detailed quantification of growth with cellular resolution indicates that the region surrounding primordia growth may have a negative growth rate [33], Figs. 2G and 3K. According to our model, this decrease of volume in boundary regions might be due to the primordium growth attracting locally most of the water supply and depriving lateral regions from water, and thus conforts the hypothesis of a new hydraulic-mechanical component of primordium lateral inhibition, beyond already identified auxin and cytokinin signals [34].

Model simplifications and further potential extensions. Throughout the development of the model, we made several key choices concerning the abstraction of a multicellular plant tissue. First, our model was developed in 2-D for reasons of computational efficiency. In principle, it can be extended in 3-D, though at the expense of more complex formalism and implementation. Second, the current model considers that water transport is performed in the plant tissue through two conceptually different pathways ([1]). Water can first move within the apoplastic compartment between the cells and finally enter a cell. Water can also move locally from cell to cell. This movement includes itself conceptually both symplasmic movements (water circulates between cells through plasmodesmata without crossing membranes) and movements from cell to cell with intermediate steps in the wall (water is for example exported locally out of the cell by water transporters like aquaporins into the wall and immediately re-imported by water transporters into neighboring cells). For sake of simplicity in this first analysis, we represented the apoplasm as a single abstract compartment able to exchange water with every cell. To analyze precisely the effect of water transporters and their genetic regulation or to assess the impact of wall resistance to water movement in the processes, explicit spatial representation of the apoplasm, of plasmodesmata and of membrane water transporters could be integrated into the model in the future.

Finally, we considered a simplified situation here by imposing constant cell osmolarity. Allowing osmolarity variations (for instance higher values in faster growing regions) may impact turgor distribution (e.g [35]). However, this should not affect the ability of the system to build up growth heterogeneities. Similarly, we further simplified our model by keeping constant the apoplastic water potential. Relaxing this hypothesis would increase cell-cell water fluxes (via the apoplasm) and could also shift the model in the direction of the flux-limiting regime. This would therefore favor regimes where growth heterogeneities are amplified by fluxes.

ACKNOWLEDGMENTS. This work has been carried out within the context of the project MecaFruit3D funded by the Agropolis foundation in Montpellier, France.

1. Cosgrove D (1986) Biophysical control of plant cell growth. Ann Rev Plant Physio 37:377–405.
2. Kutschera U (1991) Regulation of cell expansion. The cytoskeletal basis of plant growth and form pp. 85–99.
3. Cosgrove DJ (1993) Wall extensibility: its nature, measurement and relationship to plant cell growth. New Phytol 124(1):1–23.
4. Lockhart JA (1965) An analysis of irreversible plant cell elongation. J Theor Biol 8:264–275.
5. Coen E, Rolland-Lagan AG, Matthews M, Bangham JA, Prusinkiewicz P (2004) The genetics of geometry. P Natl Acad Sci USA 101(14):4728–4735.
6. Hamant O et al. (2008) Developmental Patterning by Mechanical Signals in Arabidopsis. Science 322(5908):1650–1655.
7. Alim K, Hamant O, Boudaoud A (2012) Regulatory role of cell division rules on tissue growth heterogeneity. Front Plant Sci 3:174.
8. Boudon F et al. (2015) A Computational Framework for 3D Mechanical Modeling of Plant Morphogenesis with Cellular Resolution. PLOS Comput Biol 11(1):e1003950–16.
9. Bidhendi AJ, Geitmann A (2016) Relating the mechanics of the primary plant cell wall to morphogenesis. J Exp Bot 67(2):449–461.
10. Dupuy L, Mackenzie JP, Haseloff JP (2006) A biomechanical model for the study of plant morphogenesis: Coleocheate orbicularis, a 2D study species.
11. Merks RMH, Guravage M, Inz e D, Beemster GTS (2011) VirtualLeaf: An Open-Source Framework for Cell-Based Modeling of Plant Tissue Growth and Development. Plant Physiol 155(2):656–666.
12. Dyson RJ et al. (2014) Mechanical modelling quantifies the functional importance of outer tissue layers during root elongation and bending. New Phytol 202:1212–1222.
13. Bassel GW et al. (2014) Mechanical constraints imposed by 3D cellular geometry and arrangement modulate growth patterns in the Arabidopsis embryo. P Natl Acad Sci USA 111(23):8685–8690.
14. Bozorg B, Krupinski P, Jönsson H (2016) A continuous growth model for plant tissue. Phys Biol 13(6):1–14.
15. Fozard JA, Lucas M, King JR, Jensen OE (2013) Vertex-element models for anisotropic growth of elongated plant organs. Front Plant Sci 4:233.
16. Peaucelle A et al. (2011) Pectin-induced changes in cell wall mechanics underlie organ initiation in Arabidopsis. Curr Biol 21(20):1720–1726.
17. Braybrook SA, Peaucelle A (2013) Mechano-Chemical Aspects of Organ Formation in Arabidopsis thaliana: The Relationship between Auxin and Pectin. PlOS one 8(3):e57813.
18. Sassi M et al. (2014) An Auxin-Mediated Shift toward Growth Isotropy Promotes Organ Formation at the Shoot Meristem in Arabidopsis. Curr Biol 24(19):2335–2342.
19. Jensen OE, Fozard JA (2015) Multiscale models in the biomechanics of plant growth. Physiology 30(2):159–166.
20. Cosgrove DJ (2018) Diffuse growth of plant cell walls. Plant Physiol 176:16–27.
21. Corson F et al. (2009) Turning a plant tissue into a living cell froth through isotropic growth. P Natl Acad Sci USA 106:8453–8458.
22. Long Y et al. (2018) Cellular heterogeneity in pressure and growth emerges from tissue topology and geometry. bioRxiv p. 334664.
23. Boyer JS (1988) Cell enlargement and growth-induced water potentials. Plant Physiol 73:311–316.
24. Ortega JKE (1985) Augmented growth equation for cell wall expansion. Plant Physiol 79:318–320.
25. Nobel PS (1970) Introduction to biophysical plant physiology. No. 581.1 N6.
26. Dupuy L, MacKenzie J, Rudge T, Haseloff J (2008) A system for modelling cell-cell interactions during plant morphogenesis. Ann Bot 101(8):1255–1265.
27. Kierzkowski D et al. (2012) Elastic domains regulate growth and organogenesis in the plant shoot apical meristem. Science 335(6072):1096–1099.
28. Yoon HS, Golden JW (1998) Heterocyst pattern formation controlled by a diffusible peptide. Science 282(5390):935–938.
29. Sternberg PW (1988) Lateral inhibition during vulval induction in Caenorhabditis elegans. Nature 335(6190):551–554.
30. Baker NE, Mlodzik M, Rubin GM (1990) Spacing differentiation in the developing Drosophila eye: a fibrinogen-related lateral inhibitor encoded by scabrous. Science 250(4986):1370–1377.
31. Reinhardt D et al. (2003) Regulation of phyllotaxis by polar auxin transport. Nature 426(6964):255–260.
32. Barbier de Reuille P et al. (2006) Computer simulations reveal properties of the cell-cell signaling network at the shoot apex in Arabidopsis. P Natl Acad Sci USA 103(5):1627–1632.
33. Kwiatkowska D, Dumais J (2003) Growth and morphogenesis at the vegetative shoot apex of Anagallis arvensis L. J Exp Bot 54(387):1585–1595.
34. Besnard F et al. (2014) Cytokinin signalling inhibitory fields provide robustness to phyllotaxis. Nature 505(7483):417–421.
35. Ruan YL, Llewellyn DJ, Furbank RT (2001) The control of single-celled cotton fiber elongation by developmentally reversible gating of plasmodesmata and coordinated expression of sucrose and k+ transporters and expansin. Plant Cell 13(1):47–60.

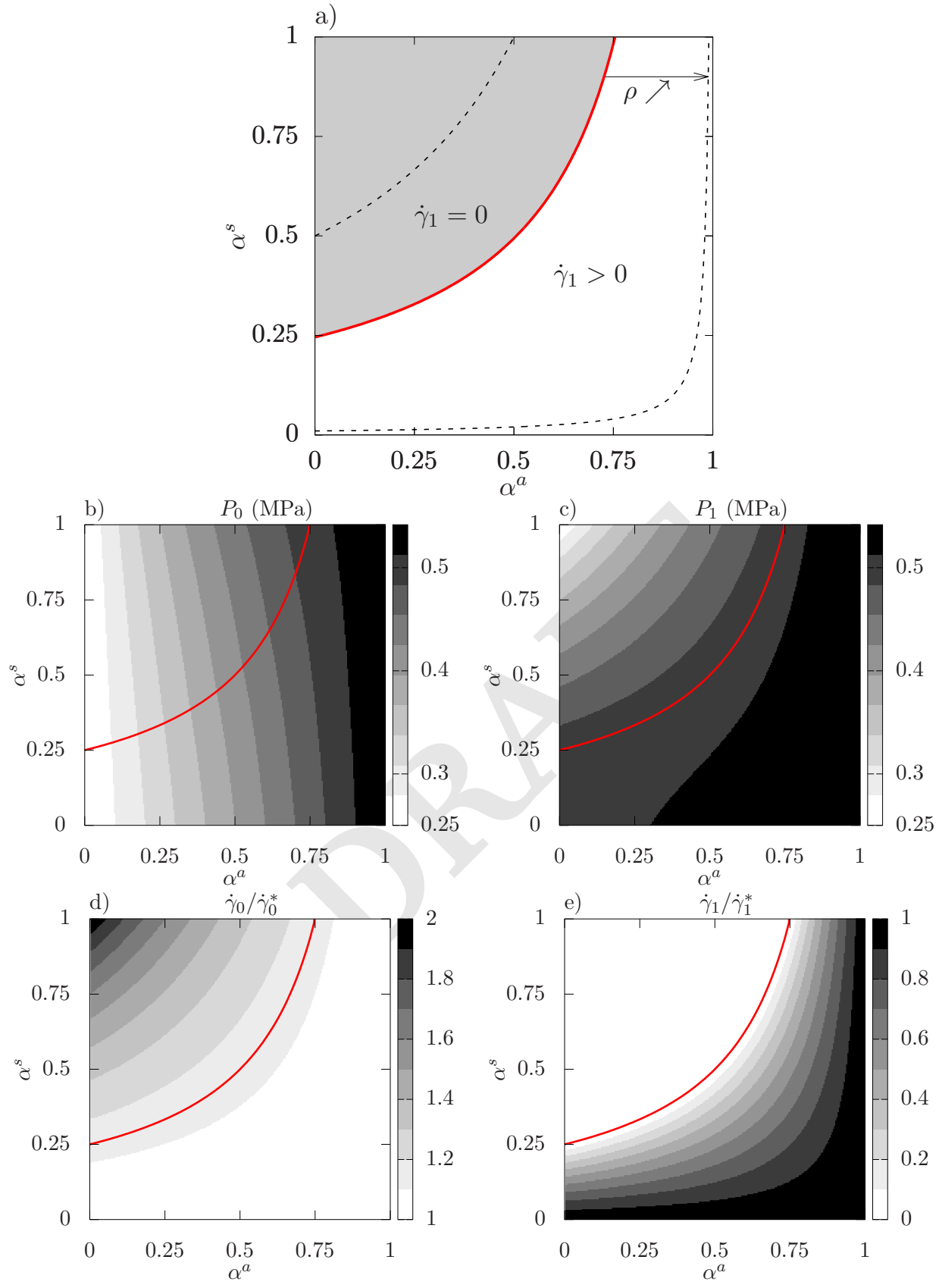

Fig. 2. Analytical resolution of the two cells model, properties of the solution in the parameters space $\alpha^a \times \alpha^s$; **a**) delimitation of the two zones $\dot{\gamma}_1 = 0$ and $\dot{\gamma}_1 > 0$: the red thick solid line $\alpha^s(\alpha^a) = \frac{1-\rho}{1-\alpha^a}$ corresponds to $\rho = 0.75$. The two black thin dashed lines correspond to the values $\rho = 0.5$ and 0.99. **b-c**) Turgors P_0 and P_1 for $\rho = 0.75$. **d-e**) relative growth rates $\dot{\gamma}_i/\dot{\gamma}_i^*$ for $\rho = 0.75$.

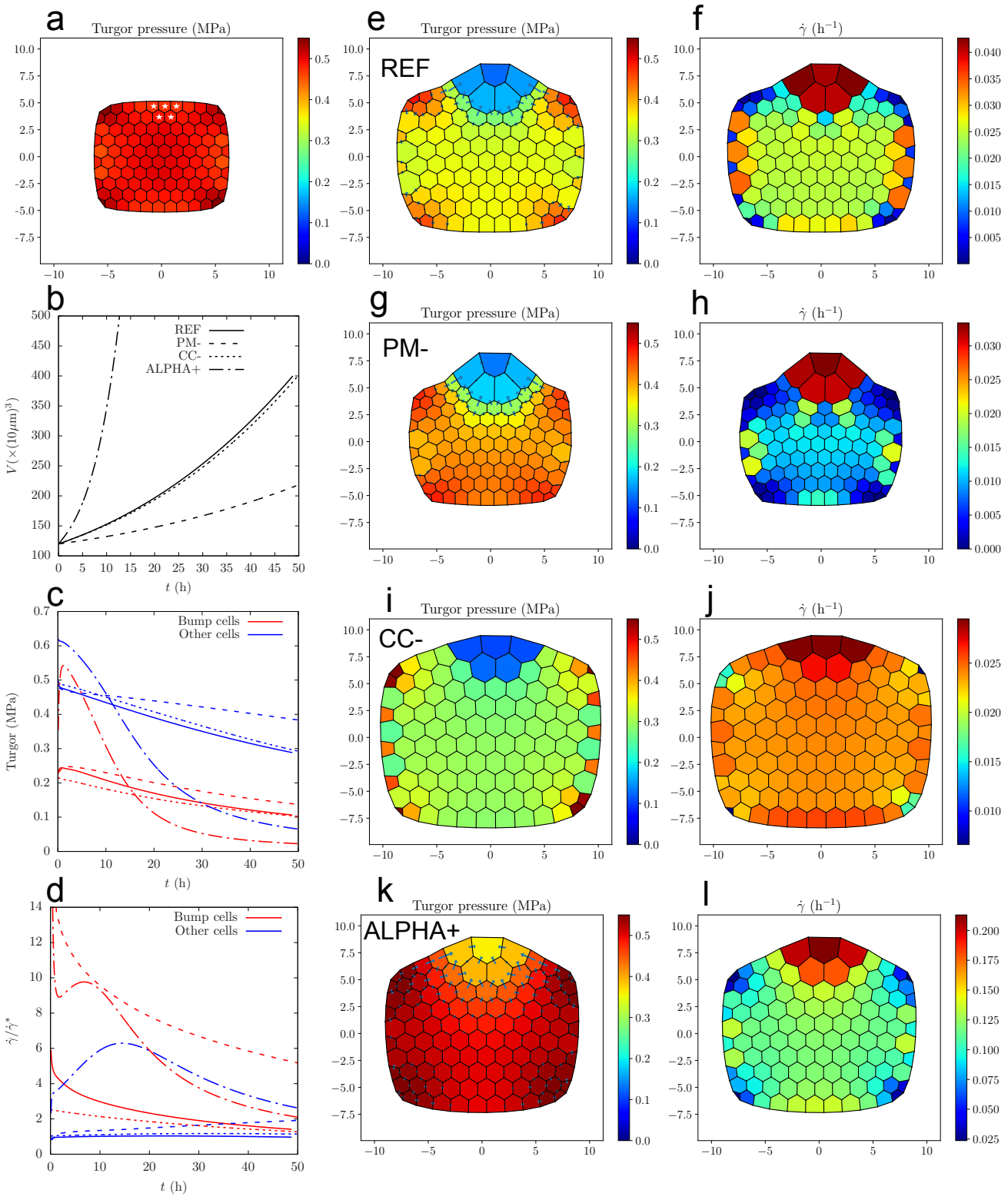

Fig. 3. Growth of tissue with heterogeneous mechanical parameters, see table 1 in SI. a) **(a)** Initial state for (REF): walls are under tension because of turgor and have reached their yield deformation. At $t = 0$, the walls of the cells marked with a white star are softened (the elastic modulus is divided by two). **(b)** Time evolution of the total volume. The dashtype of the lines distinguishes the parameters sets; the same dashtype convention is used in **(c)** and **(d)**. **(c)** Time evolution of turgor pressure of bump cells (red) and other cells (blue). **(d)** Time evolution of relative growth rate of bump cells (red) and other cells (blue). **(e-l)** Turgor and relative growth rate maps of parameters sets (REF) (**(e-f)**), (PM-) (**(g-h)**), (CC-) (**(i-j)**), and (ALPHA+) (**(k-l)**), at the time when the volume of the bump cells has increased by a factor 5: $t = 51$h for (REF), $t = 33$h for (PM-), $t = 80$h for (CC-), $t = 14.8$h for (ALPHA+). The arrows represent the intensity and direction of cell-cell water fluxes; the scale for arrows is the same for (REF), (PM-) and (CC-) and close to 4 times higher for (ALPHA+).

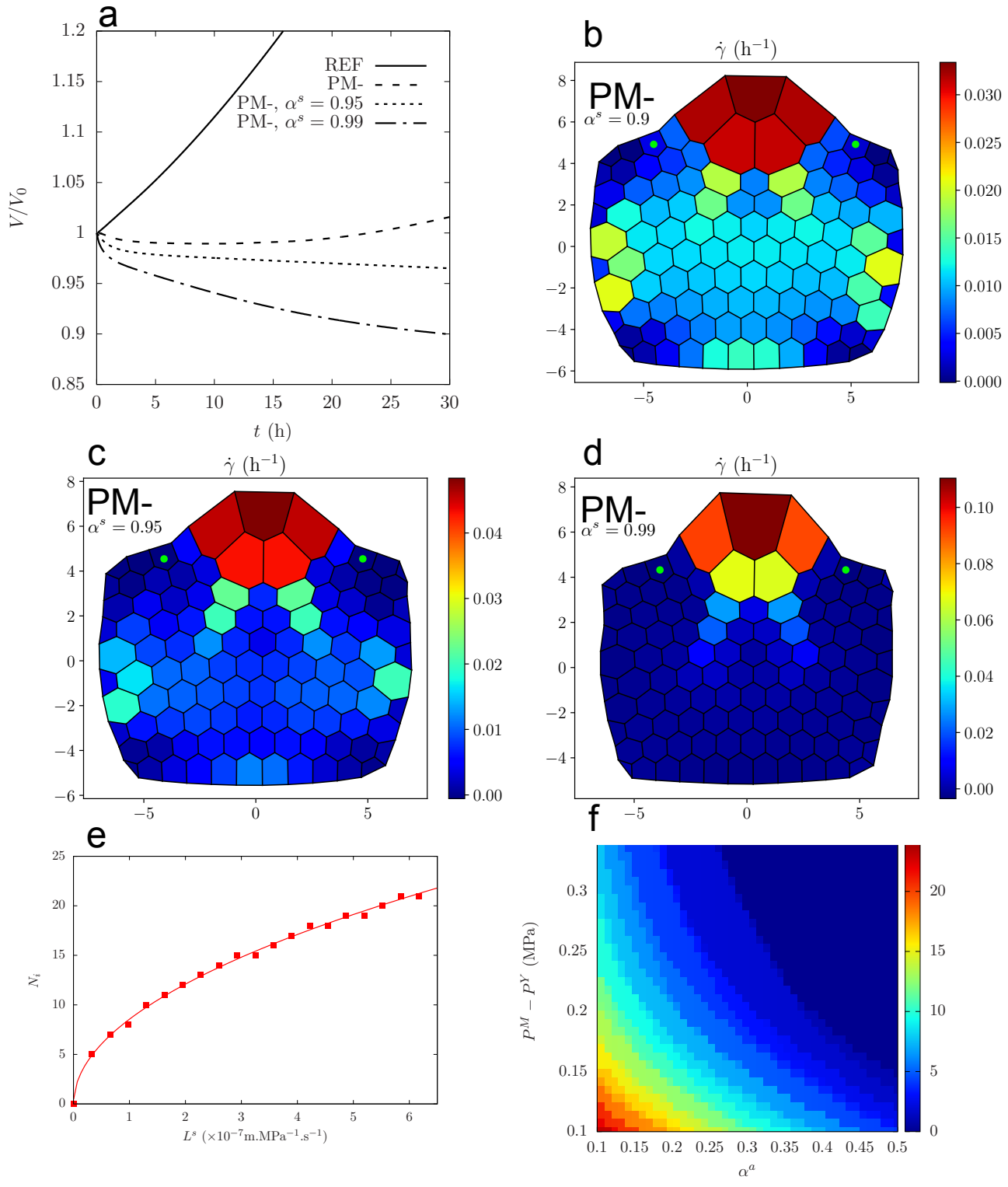

Fig. 4. Evidence of lateral inhibition: left: **a**) time evolution of the volume of two cells on the boundary of the bump (marked with a green dot on the maps **b, c, d**) with the sets of parameters (REF), (PM-), (PM-) with $\alpha^s = 0.95$, (PM-) with $\alpha^s = 0.99$. V_0 is the volume of the cells at $t = 0$. **b,c,d**) maps of relative growth rate at $t = 33$h for (PM-), $t = 20$h for (PM-) and $\alpha^s = 0.95$, $t = 10$h for (PM-) and $\alpha^s = 0.99$. **e-f**) Results for a chain of $2N + 1$ cells with $N = 50$, where the central cell has twice softer walls; **e**) number N_i of cells that are inhibited on each side of the central cell, for different values of L^s; the line is a fit with a square root function, in the form $c\sqrt{L^s}$. **f**) Values of the prefactor c in the space (α^a, P^M).

PNAS
www.pnas.org

Supplementary Information for

Coupling water fluxes with cell wall mechanics in a multicellular model of plant development

Ibrahim Cheddadi, Michel Génard, Nadia Bertin, Christophe Godin

Corresponding authors: Ibrahim Cheddadi and Christophe Godin.
E-mail: ibrahim.cheddadi@univ-grenoble-alpes.fr, christophe.godin@inria.fr

This PDF file includes:

Supporting Information Text

1. Calculations for simplified models

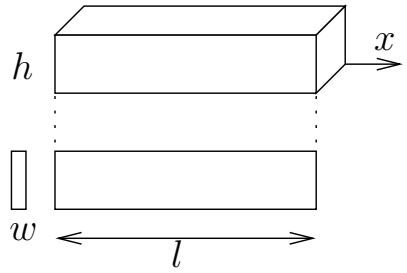

Fig. S1. Geometrical parameters of Lockhart-Ortega models: height h and length l of the cell, thickness w of the walls. The two faces orthogonal to the x axis are refered to as base faces while the four other faces are refered to as lateral faces.

Lockhart-Ortega models. The equations of cell wall elongation (Eq. (1) in main text) and of water uptake (Eq. 2 in main text) can be linked thanks to the geometry of the cell and the mechanical equilibrium. See Fig. S1 for the geometrical description.

First, the cell volume is $V = h^2 l$ and therefore we find that the relative growth rate of the cell is equal to the strain rate of the walls:

$$\dot{\gamma} = \frac{1}{V}\frac{\mathrm{d}V}{\mathrm{d}t} = \frac{1}{l}\frac{\mathrm{d}l}{\mathrm{d}t} = \dot{\varepsilon}. \qquad [S1]$$

Then, we consider the balance of forces on the base faces (see Fig. S1 for the nomenclature); their area is $h \times h$ and they are submitted to a total pressure force Ph^2 in the direction of the main axis of the cell, balanced by the tension from the lateral walls. Let σ be the common (scalar) stress in the walls; the wall thickness is w so their cross section is $h \times w$ and therefore they each exert a force σhw on the base faces. To be coherent with the bidimensional model we propose, we consider that the top and bottom lateral faces bear no stress and the balance of forces leads to

$$Ph^2 = 2\sigma hw$$

and therefore the balance of forces leads to $P = 2\frac{w}{h}\sigma$. Finally, thanks to this equation and the identity Eq. (S1), the Lockhart-Ortega model (eqs. (1), (3) in main text) is reduced to the following differential equation for P:

$$\frac{1}{\bar{E}}\frac{\mathrm{d}P}{\mathrm{d}t} + \phi^w (P - P^Y)_+ = \phi^a \left(P^M - P\right), \qquad [S2]$$

where $\phi^a = \frac{AL^a}{V}$ has been introduced in the main text; in order to keep the calculations as simple as possible, Lockhart made the assumption that the area of the base faces is negligeable compared to the area $A = 4hl$ of the lateral faces (see Fig. S1). Note that the cell volume is $V = h^2 l$ and therefore the ratio $A/V = 4/h$ is constant.

Let's study the transient behaviour of equation Eq. (S2), from an initial condition $P(t = 0) = 0$:

- Elastic regime: first, P is below P^Y and the plastic rate is zero; Eq. (S2) becomes

$$\lambda^a \frac{\mathrm{d}P}{\mathrm{d}t} + P = P^M,$$

  where $\lambda^a = \frac{1}{\phi^a \bar{E}}$ is a characteristic time. The solution is

$$P = P^M(1 - \exp(-t/\lambda^a)).$$

  The relative growth rate is

$$\dot{\gamma} = \phi^a P^M \exp(-t/\lambda^a).$$

- Plastic regime: the plastic regime starts when $P = P^Y$, at $t^0 = \lambda^a \log\left(\frac{P^M}{P^M - P^Y}\right)$. The equation Eq. (S2) becomes:

$$\frac{1}{\bar{E}}\frac{\mathrm{d}P}{\mathrm{d}t} + (\phi^a + \phi^w)P = \phi^a P^M + \phi^w P^Y,$$

and equivalently

$$\lambda^{aw}\frac{\mathrm{d}P}{\mathrm{d}t} + P = \alpha^a P^M + (1 - \alpha^a)P^Y,$$

where $\lambda^{aw} = \frac{1}{(\phi^a+\phi^w)\bar{E}}$ is a characteristic time. The solution is

$$P = \alpha^a P^M + (1-\alpha^a)P^Y - \alpha^a(P^M - P^Y)\exp((t^0-t)/\lambda^{aw}), \quad [S3]$$

$$\dot{\gamma} = \frac{\phi^a\phi^w}{\phi^a+\phi^w}(P^M - P^Y) - \frac{(\phi^a)^2}{\phi^a+\phi^w}(P^M - P^Y)\exp((t^0-t)/\lambda^{aw}). \quad [S4]$$

The stationnary solution is

$$P^* = \alpha^a P^M + (1-\alpha^a)P^Y \quad [S5]$$

$$\dot{\gamma}^* = \frac{\phi^a\phi^w}{\phi^a+\phi^w}(P^M - P^Y). \quad [S6]$$

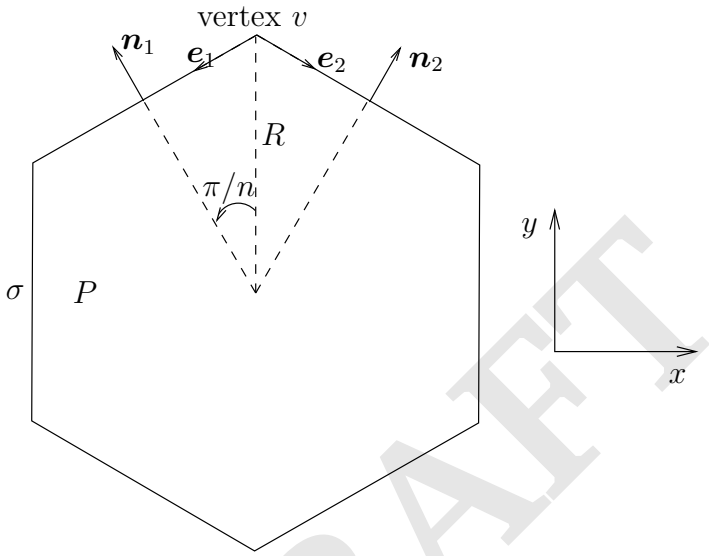

Fig. S2. Geometrical parameters for the single polygonal cell model.

Single polygonal cell. We consider a regular convex polygon of radius R with n edges that represents a cell (see Fig. S2).

Mechanical equilibrium. Let σ be the stress in the walls and P the pressure inside the cell; the outside pressure is set to zero. The length of the edges is $2R\sin(\pi/n)$, and the walls are given a height h and a thickness w; therefore the stresses are exerted on a surface hw; the contribution of pressure on vertex v is $\frac{1}{2}P2hR\sin(\pi/n)(\boldsymbol{n}_1+\boldsymbol{n}_2)$. Therefore, the balance of forces on vertex v writes:

$$\frac{1}{2}P2hR\sin(\pi/n)(\boldsymbol{n}_1+\boldsymbol{n}_2) + \sigma hw(\boldsymbol{e}_1+\boldsymbol{e}_2) = 0.$$

The normal vectors are

$$\boldsymbol{n}_1 = (-\sin(\pi/n), \cos(\pi/n)) \quad \text{and} \quad \boldsymbol{n}_2 = (\sin(\pi/n), \cos(\pi/n)).$$

The tangent vectors are

$$\boldsymbol{e}_1 = (-\cos(\pi/n), -\sin(\pi/n)) \quad \text{and} \quad \boldsymbol{e}_2 = (\cos(\pi/n), -\sin(\pi/n)).$$

By symetry, the x component of the resulting force is zero; the projection of the balance of forces on y axis yields

$$2PhR\sin(\pi/n)\cos(\pi/n) - 2\sigma hw\sin(\pi/n) = 0,$$

and

$$P = \frac{w}{R\cos(\pi/n)}\sigma. \quad [S7]$$

When $n \to \infty$, $\cos(\pi/n) \to 1$ and we recover the Laplace law.

Flux equation. The surface of the polygon is

$$S_n = n \times 2R\sin(\pi/n)R\cos(\pi/n)/2 = R^2 n \sin(\pi/n)\cos(\pi/n).$$

The volume of the cell is $V = S_n h$, so the volume variation is

$$\frac{\mathrm{d}V}{\mathrm{d}t} = 2hR\frac{\mathrm{d}R}{\mathrm{d}t} n \sin(\pi/n)\cos(\pi/n).$$

The perimeter of the polygon is $n \times 2R\sin(\pi/n)$ so the lateral area of the cell is

$$A = 2nhR\sin(\pi/n).$$

Note that the ratio A/V is not constant:

$$\frac{A}{V} = \frac{2}{R\cos(\pi/n)}.$$

Finally, the flux equation writes

$$2hR\frac{\mathrm{d}R}{\mathrm{d}t} n \sin(\pi/n)\cos(\pi/n) = n2hR\sin(\pi/n)L(P^M - P),$$

which yields

$$\frac{\mathrm{d}R}{\mathrm{d}t} = \frac{L}{\cos(\pi/n)}(P^M - P) \quad [S8]$$

Wall rheology. Let ε^e be the elastic deformation of the walls; it is related to the stress by the constitutive equation $\sigma = E\varepsilon^e$ where E is the elastic modulus. The length of the edges is $l = 2R\sin(\pi/n)$ and therefore the strain rate of the edges is $\frac{1}{l}\frac{\mathrm{d}l}{\mathrm{d}t} = \frac{1}{R}\frac{\mathrm{d}R}{\mathrm{d}t}$. The rheological behaviour of the walls is given by

$$\frac{1}{R}\frac{\mathrm{d}R}{\mathrm{d}t} = \frac{\mathrm{d}\varepsilon^e}{\mathrm{d}t} + \Phi^w E \max(0, \varepsilon^e - \varepsilon^Y), \quad [S9]$$

or equivalently

$$\frac{1}{R}\frac{\mathrm{d}R}{\mathrm{d}t} = \frac{1}{E}\frac{\mathrm{d}\sigma}{\mathrm{d}t} + \Phi^w \max(0, \sigma - \sigma^Y), \quad [S10]$$

where ε^Y (resp. σ^Y) is a yield elastic deformation (resp. stress).

Numerical results. The problem to solve is reduced to a set of two differential equations. It is numerically solved with the `odeint` routine from the `python` library `scipy`.

We study the growth of a hexagonal cell ($n = 6$) growing from an initial state where the elastic deformation of the walls is set to the threshold value, in order to bypass the pure elastic regime; computations are run over a long time scale. We want to study how this models compares to Lockhart-Ortega when the relative importance of fluxes and wall synthesis varies; to this end, we run three simulations with $\alpha^a = 0.1, 0.5, 0.9$. Let $R_0 = 10\mu$m be the initial radius of the cell, then $P^Y = \frac{w}{R_0\cos(\pi/6)}E\varepsilon^Y$ is a representative value for the yield turgor of a hexagonal cell. The value $\varepsilon^Y = 0.1$ is chosen accordingly to experimental observations where wall deformations can be of the order of 10%; then we choose E such that $P^Y = 0.5$ MPa, which sets an order of magnitude for the initial turgor of the cell, close to observed experimental data. We choose $P^M = 0.7$ MPa so that it is above P^Y. Finally, we can use the Lockhart's prediction Eq. (S6) as an order of magnitude of the relative growth rate; we choose $\dot{\gamma}^* = 2\% \cdot \mathrm{h}^{-1}$. Then, a given value of α^a (evaluated with the initial area of the cell) sets a unique value of L^a and ϕ^w.

At the onset of the simulation, walls start to extend irreversibly and plastic growth occurs. Fig. S3a,c shows that the volume increases faster for large values of α^a, although we have chosen the parameters so that the Lockhart model predicts a constant and common value of $\dot{\gamma}$. Fig. S3b shows that P is initially close to Lockhart predictions P^* but decreases fastly to zero; the fast decrease of P coincides with peaks of $\dot{\gamma}$ (Fig. S3c) above the value $\dot{\gamma}^*$ with a higher peak for larger values of α^a; the elastic deformation ε^e (Fig. S3d)is not constant either, with a large peak above the Lockhart-Ortega prediction for $\alpha^a = 0.9$. For all values of α^a, ε^e converges toward the threshold ε^Y.

Two-cells model. The geometry and notations of the two-cells model is recalled in Fig. S4. Gathering the flux equation (Eq. 8 from main text) and the wall mechanics equation (Eq. 1 from main text) with $\frac{\mathrm{d}P}{\mathrm{d}t} = 0$, we get

$$\phi^a(P^M - P_0) + \frac{\phi^s}{2}(P_1 - P_0) - \phi^w(P_0 - P_0^Y)_+ = 0 \quad [S11]$$

$$\phi^a(P^M - P_1) - \frac{\phi^s}{2}(P_1 - P_0) - \phi^w(P_1 - P_1^Y)_+ = 0. \quad [S12]$$

First, we assume that both cells are growing ($P_i > P_i^Y, i = 0, 1$).

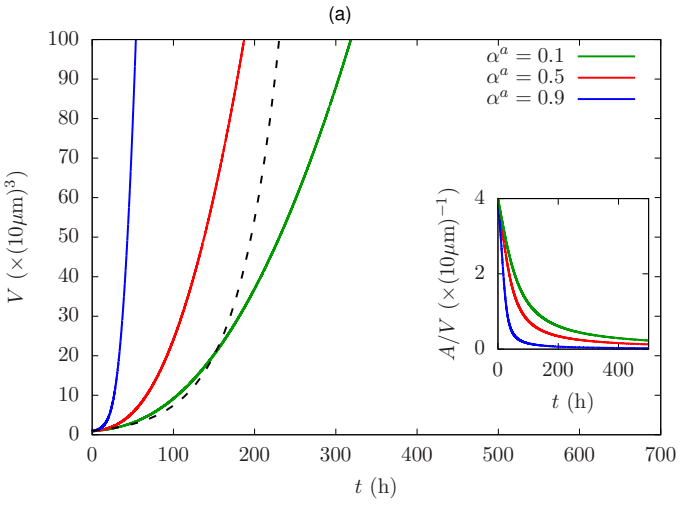

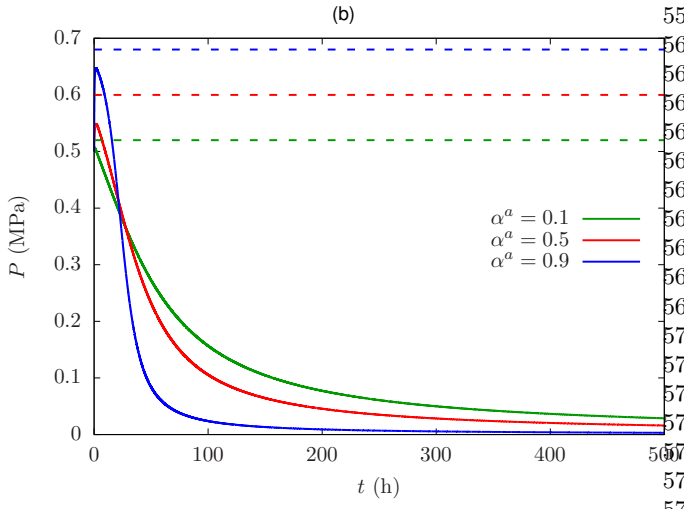

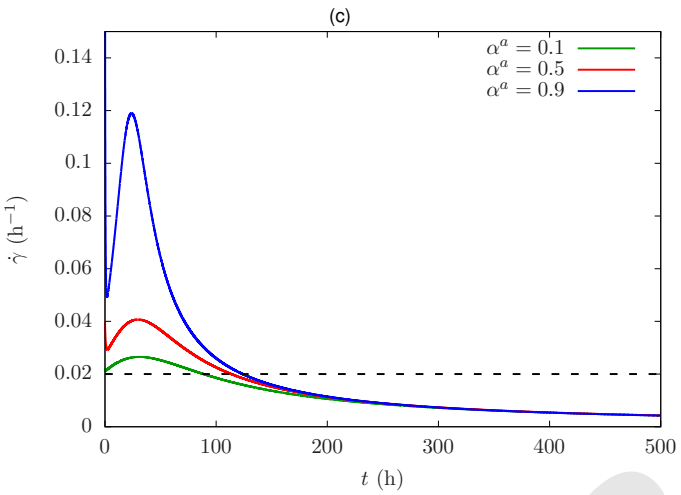

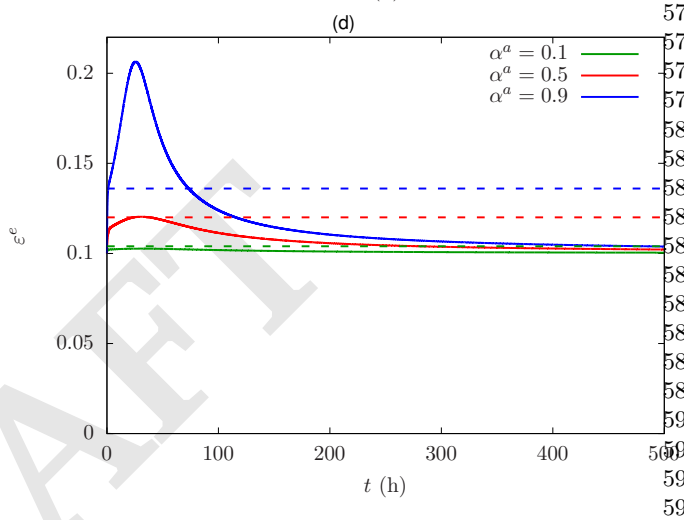

Fig. S3. Growth of a single hexagonal cell for three different values of α^a: time evolution of volume (inset: ratio area/volume) (a), turgor (b), relative growth rate (c), and elastic deformation of the walls (d). The dashed lines correspond to the solution of the Lockhart model; note that the chosen sets of parameters lead to the constant and equal value $\dot{\gamma}^* = 2\% \cdot \text{h}^{-1}$, and to the same evolution of volume.

First regime: $P_i > P_i^Y, i = 0, 1.$ Adding Eq. (S11) and Eq. (S12) we get:

$$\overline{P} = \alpha^a P^M + (1 - \alpha^a)\overline{P}^Y, \qquad \text{[S13]}$$

where $\alpha^a = \dfrac{\phi^a}{\phi^a + \phi^w}$, $\overline{P} = \dfrac{P_0 + P_1}{2}$. With Eq. 1 from main text, we get

$$\overline{\dot{\gamma}} = \frac{\phi^a \phi^w}{\phi^a + \phi^w}(P^M - \overline{P}^Y), \qquad \text{[S14]}$$

where $\overline{\dot{\gamma}} = \frac{\dot{\gamma}_0 + \dot{\gamma}_1}{2}$ Therefore, the gathering of two cells behaves the same as one cell if one considers the mean values.

Then, we examine the heterogeneities in turgor and growth rate. Substracting Eq. (S11) to Eq. (S12), we get

$$\Delta P = \frac{\phi^w}{\phi^a + \phi^s + \phi^w}\Delta P^Y.$$

Let

$$\alpha^s = \frac{\phi^s}{\phi^s + \phi^a}.$$

Then the previous expression becomes

$$\Delta P = \frac{(1 - \alpha^a)(1 - \alpha^s)}{1 - \alpha^s + \alpha^a \alpha^s}\Delta P^Y. \qquad \text{[S15]}$$

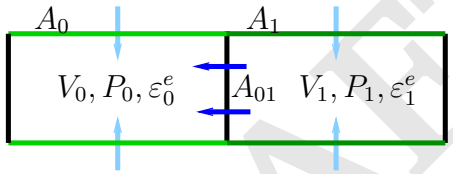

Fig. S4. Two cells model: symplasmic flows (dark blue arrows) occur through the contact surface A_{01}; apoplasmic flows (light blue arrows) occur through the surfaces A_0 and A_1. Growth is restricted to the green edges: cell 0 (in dark green) has stiffer walls that cell 1 (in light green).

As $(1-\alpha^a)(1-\alpha^s) = 1-\alpha^a-\alpha^s+\alpha^a\alpha^s < 1-\alpha^s+\alpha^a\alpha^s$, we find that turgor difference ΔP cannot exceed the value ΔP^Y. When $\alpha^s = 0$ (symplasmic fluxes negligeable with respect to apoplasmic ones), then $\Delta P = (1-\alpha^a)\Delta P^Y$; when $\alpha^s > 0$, symplasmic fluxes tend to reduce the turgor heterogeneity between cells.

With Eq. 7 from main text we get then

$$\Delta\dot{\gamma} = \frac{(\phi^a+\phi^s)\phi^w}{\phi^a+\phi^s+\phi^w}\Delta P^Y, \tag{S16}$$

where $\Delta\dot{\gamma} = \frac{\dot{\gamma}_0-\dot{\gamma}_1}{2}$. Note that this expression is valid iff $P_1 > P_1^Y$ or equivalently $\dot{\gamma}_1 > 0$. The limit $\dot{\gamma}_1 = 0$ corresponds to the situation where cell 0 is growing in such a way that it prevents cell 1 to grow because of the symplasmic fluxes between them. We examine how this situation can occur depending on the values of the sumplasmic conductivity ϕ^s and the other parameters. We find that

$$\begin{aligned} P_1 > P_1^Y &\iff \frac{\phi^a+\phi^s}{\phi^a+\phi^s+\phi^w}\frac{\Delta P^Y}{P^M-\overline{P}^Y} < \frac{\phi^a}{\phi^a+\phi^w} \\ &\iff \frac{\alpha^a}{1-(1-\alpha^s)\alpha^a}\rho < \alpha^a \\ &\iff \alpha^s < \frac{1-\rho}{1-\alpha^a}. \end{aligned}$$

For instance, $P_0^Y = 0.25$ MPa, $P_1^Y = 0.5$ MPa, and $P^M = 0.625$ MPa yields $\rho = 0.5$. The hypothesis of this study ($P_0^Y < P_1^Y < P^M$) corresponds to the condition $\rho \in [0,1]$. Note that if $\alpha^a > \rho$, then $\frac{1-\rho}{1-\alpha^a} > 1$, and the condition is verified whatever the value of α^s; if $\alpha^s = 1-\rho$, the condition is equivalent to $\alpha^a > 0$, which is also always verified. Fig. S4a) recapitulates the regions of the parameters space $\alpha^a \times \alpha_s$ where the condition is verified, for different values of ρ. The size of the region $\dot{\gamma}_1 = 0$ increases as ρ gets closer to 1.

Second regime: $P_0 > P_0^Y$ and $P_1 < P_1^Y$. In this case, eqs. Eq. (S11) and Eq. (S12) turn into

$$\phi^a(P^M-P_0) + \frac{\phi^s}{2}(P_1-P_0) - \phi^w(P_0-P_0^Y) = 0 \tag{S17}$$

$$\phi^a(P^M-P_1) - \frac{\phi^s}{2}(P_1-P_0) = 0. \tag{S18}$$

Eq. (S18) leads to

$$P_1 = (1-\tilde{\alpha}^s)P^M + \tilde{\alpha}^s P_0, \tag{S19}$$

where $\tilde{\alpha}^s = \frac{\phi^s}{2\phi^a+\phi^s}$. Adding eqs. Eq. (S17) and Eq. (S18) leads to

$$P_0(\phi^a+\phi^w) = 2\phi^a P^M + \phi^w P_0^Y - \phi^a((1-\tilde{\alpha}^s)P^M + \tilde{\alpha}^s P_0),$$

then,

$$P_0(\phi^a(1+\tilde{\alpha}^s)+\phi^w) = \phi^a(1+\tilde{\alpha}^s)P^M + \phi^w P_0^Y,$$

and finally

$$P_0 = \alpha^{as}P^M + (1-\alpha^{as})P_0^Y, \tag{S20}$$

where

$$\alpha^{as} = \frac{\phi^{as}}{\phi^{as}+\phi^w} \qquad \text{and} \qquad \phi^{as} = \phi^a(1+\tilde{\alpha}^s).$$

Hence, thanks to the symplasmic fluxes from its neighbour cell 1, cell 0 benefits from an enhanced access to the apoplasmic fluxes by a factor $\phi^{as}/\phi^a = 1+\tilde{\alpha}^s$. Then, from Eq. 1 in main text, the relative growth rate of cell 0 is

$$\dot{\gamma}_0 = \frac{\phi^{as}\phi^w}{\phi^{as}+\phi^w}(P^M-P_0^Y). \tag{S21}$$

By hypothesis, the growth rate of cell 1 is zero, and we can compute the heterogeneity in turgor: from Eq. (S19), we find that

$$\Delta P = \frac{1-\tilde{\alpha}^s}{2}(P^M-P_0),$$

and hence

$$\Delta P = \frac{1}{2}(1-\tilde{\alpha}^s)(1-\alpha^{as})(P^M-P_0^Y). \tag{S22}$$

2. Numerical resolution of the 2D multicellular model

Structure of the mathematical problem. Thanks to the geometrical constraint of uni-directional growth, the Lockhart-Ortega is very simple to resolve. The identity between the relative growth rate of the cell and the strain rate of the walls allows to couple the equation that describes fluxes, and the equation that describes walls synthesis. Then the stress in the walls and the pressure inside the cell are linked by the mechanical equilibrium. Finally there is only one independent variable (pressure for instance) and the model can be solved analytically.

Conversely, in the bidimensionnal model we propose, the properties of a given wall (elongation rate and elastic deformation) cannot be directly linked to the properties of the adjacent cells (growth rate and pressure). Hence a new strategy has to be developped. First, we emphasize the strong coupling between fluxes and mechanics: the motion of the vertices is prescribed by the mechanical equilibrium (Eq. 11 from main text) between pressure forces and elastic forces; meanwhile, a displacement of the vertices can cause a variation of volume of several cells, which has to be balanced by water fluxes (Eq. 10 from main text); water fluxes are limited by the finite permeability of the walls, which sets a constraint on possible variations of volume. Similarly, any variation in the length of the walls leads to a modification of their elastic deformation (Eq. 7 from main text).

Another way to understand this problem is to consider it as the minimization of mechanical energy (mechanical equilibrium Eq. 11 from main text) under two constraints on the position of the vertices, through the volumes of the cells (Eq. 10 from main text) and the lengths of the edges (Eq. 7 from main text). This kind of problem is often encountered in mechanics, *e.g* solid friction, contact mechanics, or incompressible fluid mechanics; a powerfull theoritical and practical tool to solve this is the method of lagrangian multipliers. For instance, in the context of incompressible fluid mechanics, the constraint of volume conservation is relaxed by pressure that acts as a lagragian multiplier. Physically, the pressure adjusts itself so that both the constraint and the mechanical equilibrium are satisfied. The model we propose exhibits the same structure, as pressure will adjust to both fluxes and mechanical constraints. However, the system here is discrete, and the flux equation (Eq. 10 in main text) is linear with respect to pressure, so it can be reduced to a linear system. We will take advantage of this for the resolution of the model.

Resolution algorithm.

Volumes and lengths as functions of the positions of the vertices. First, we express volumes and lengths as functions of the positions of the vertices. Let N_v be the number of vertices and $\boldsymbol{X} \in \mathbb{R}^{2N_v}$ the vector of the positions of all the vertices. The volume of a cell i is $V_i = S_i h$ where S_i is its surface. As cells are non intersecting polygons, their signed surface is given by the general formula

$$S_i = \frac{1}{2}\sum_{k=0}^{n_i-1}(x_k y_{k+1} - x_{k+1}y_k), \tag{S23}$$

where n_i is the number of vertices of cell i, $(x_k, y_k)_{k=0,\dots,n_i-1}$ are the coordinates of the vertices of the cell i in counterclockwise order, and we set $(x_{n_i}, y_{n_i}) = (x_0, y_0)$. Let N_c be the number of cells and $\boldsymbol{V} \in \mathbb{R}^{N_c}$ the vector of all the cells volumes; thanks to Eq. (S23), it can be expressed as a function of $\boldsymbol{X}$ and its gradient $\nabla_{\boldsymbol{X}}\boldsymbol{V}$ with respect to $\boldsymbol{X}$ can be computed. Then the time derivative of $\boldsymbol{V}$ expresses as

$$\frac{\mathrm{d}\boldsymbol{V}}{\mathrm{d}t} = \nabla_{\boldsymbol{X}}\boldsymbol{V}\frac{\mathrm{d}\boldsymbol{X}}{\mathrm{d}t}.$$

Note here that $\nabla_{\boldsymbol{X}}\boldsymbol{V}$ is a $N_c \times 2N_e$ matrix and $\frac{\mathrm{d}\boldsymbol{X}}{\mathrm{d}t}$ is a $2N_e$ vector, so their product is well defined and has the correct dimension.

Similarly, the length of a segment k with two vertices $v_1 = (x_1, y_1)$ and $v_2 = (x_2, y_2)$ at its ends is

$$l_k = \sqrt{(x_1 - x_2)^2 + (y_1 - y_2)^2}. \tag{S24}$$

Let N_e be the number of edges and $\boldsymbol{l} \in \mathbb{R}^{N_e}$ the vector of all the edges lengths; thanks to Eq. (S24), it can be expressed as a function of $\boldsymbol{X}$ and its gradient $\nabla_{\boldsymbol{X}}\boldsymbol{l}$ with respect to $\boldsymbol{X}$ can be computed. Then the time derivative of $\boldsymbol{l}$ expresses as

$$\frac{\mathrm{d}\boldsymbol{l}}{\mathrm{d}t} = \nabla_{\boldsymbol{X}}\boldsymbol{l}\frac{\mathrm{d}\boldsymbol{X}}{\mathrm{d}t}.$$

Time discretisation. Time is discretized using a fixed time step Δt and the time derivatives are approximated by the 1st order Euler scheme, for instance:

$$\frac{\mathrm{d}\boldsymbol{X}}{\mathrm{d}t}(t) \approx \frac{\boldsymbol{X}(t+\Delta t) - \boldsymbol{X}(t)}{\Delta t}.$$

Let $\boldsymbol{\varepsilon} \in \mathbb{R}^{N_e}$ be the vector of all the elastic deformations of the edges. Let $\boldsymbol{X}^0 = \boldsymbol{X}(0)$ and $\boldsymbol{\varepsilon}^0 = \boldsymbol{\varepsilon}(0)$ be some initial conditions. We construct successive approximations of the solution at times $t_n = n\Delta t$ for $n > 0$ by solving at each time step the mechanical equilibrium (Eq. 11 from main text) along with the discretized versions of flux (Eq. 10 from main text) and wall rheology (Eq. 7 from main text) equations: let $\boldsymbol{P} \in \mathbb{R}^{N_c}$ be the vector of all the cells pressures; these equations can be written in a matrix form:

$$\nabla_{\boldsymbol{X}}\boldsymbol{V}(\boldsymbol{X}^{n+1})\frac{\boldsymbol{X}^{n+1} - \boldsymbol{X}^n}{\Delta t} = M_P\boldsymbol{P}^{n+1} + \boldsymbol{b}_P, \tag{S25}$$

$$\frac{\boldsymbol{\varepsilon}^{n+1} - \boldsymbol{\varepsilon}^n}{\Delta t} + \boldsymbol{\beta}^n\boldsymbol{\varepsilon}^{n+1} = \frac{1}{\boldsymbol{l}(\boldsymbol{X}^{n+1})}\nabla_{\boldsymbol{X}}\boldsymbol{l}(\boldsymbol{X}^{n+1})\frac{\boldsymbol{X}^{n+1} - \boldsymbol{X}^n}{\Delta t}. \tag{S26}$$

where M_P is a $N_i \times N_i$ matrix, with the following non-zero coefficients:

$$M_P(i,i) = A_i L_i^a - \sum_{j \in n(i)} A_{ij} L_{ij}^s, \qquad \forall i = 1, \dots, N_c,$$
$$M_P(i,j) = A_{ij} L_{ij}^s, \quad \forall i = 1, \dots, N_c, \qquad \forall j \in n(i),$$

with $\boldsymbol{b}_P \in \mathbb{R}^{N_c}$ is defined by its coefficients

$$\boldsymbol{b}_p(i) = A_i L_i^a P^M, \qquad \forall i = 1, \dots, N_c.$$

Note here that the model implies no time derivative of the pressure, so that $\forall n > 0$, $\boldsymbol{P}^{n+1}$ can be computed without the knowledge of $\boldsymbol{P}^n$, and the initial value of the pressure is not needed.

In addition, $\boldsymbol{\beta}^n$ is the $N_e \times N_e$ diagonal matrix with components $\boldsymbol{\beta}^n(k,k) = \frac{2w}{h} \phi_k^w E_k \max\left(0, \frac{\varepsilon_k^n - \varepsilon_k^Y}{\varepsilon_k^n}\right)$ for $k = 1, \dots, N_e$, and for the purpose of notation, $\frac{1}{\boldsymbol{l}}$ is the $N_e \times N_e$ diagonal matrix with components $1/l_k$. Note here that the variables $\boldsymbol{\beta}^n$ are taken at time step n so that they are considered as constants at time step $n+1$ and the equation Eq. (S26) is linear with respect to the unknown $\boldsymbol{\varepsilon}^{n+1}$.

Pressure and elastic deformation as functions of the position of the vertices. Thanks to this time discretization, we see that at each time step, the unknown pressure $\boldsymbol{P}^{n+1}$ and elastic deformation $\boldsymbol{\varepsilon}^{n+1}$ are defined through the linear equations Eq. (S25) and Eq. (S26) which can be easily inverted, which allows to express both these variables as functions of the spatial unknown $\boldsymbol{X}^{n+1}$.

First, from equation Eq. (S25):

$$P(\boldsymbol{X}^{n+1}) = \frac{1}{\Delta t} M_P^{-1} \nabla_{\boldsymbol{X}} \boldsymbol{V}(\boldsymbol{X}^{n+1}) \boldsymbol{X}^{n+1} - M_P^{-1} \left(\frac{1}{\Delta t} \nabla_{\boldsymbol{X}} \boldsymbol{V}(\boldsymbol{X}^{n+1}) \boldsymbol{X}^n - \boldsymbol{b}_P \right). \quad \text{[S27]}$$

Then, using Eq. (S26):

$$\boldsymbol{\varepsilon}\left(\boldsymbol{X}^{n+1}\right) = \frac{1}{\Delta t} M_\varepsilon^{-1} \frac{1}{\boldsymbol{l}(\boldsymbol{X}^{n+1})} \nabla_{\boldsymbol{X}} \boldsymbol{l}(\boldsymbol{X}^{n+1}) \boldsymbol{X}^{n+1} - \frac{1}{\Delta t} M_\varepsilon^{-1} \left(\frac{1}{\boldsymbol{l}(\boldsymbol{X}^{n+1})} \nabla_{\boldsymbol{X}} \boldsymbol{l}(\boldsymbol{X}^{n+1}) \boldsymbol{X}^n - \boldsymbol{\varepsilon}^n \right), \quad \text{[S28]}$$

where $M_\varepsilon = \frac{1}{\Delta t} I_{N_e} + \boldsymbol{\beta}^n$.

Structure of the resolution algorithm Thanks to the two previous steps, we are now able to propose a algorithm for the resolution of the model.

- Initialization: Define $\boldsymbol{X}^0 \in \mathbb{R}^{2N_v}$ and $\boldsymbol{\varepsilon}^0 \in \mathbb{R}^{N_e}$
- $\forall n \geq 0$, assuming $\boldsymbol{X}^n$ and $\boldsymbol{\varepsilon}^n$ are known, let $\boldsymbol{F}^n : \mathbb{R}^{2N_v} \to \mathbb{R}^{2N_v}$ be the function such that $\forall v = 0, \dots, N_v - 1$,

$$\begin{pmatrix} F_{2v+1}^n(\boldsymbol{X}) \\ F_{2v+2}^n(\boldsymbol{X}) \end{pmatrix} = \frac{1}{2} \sum_{k \in f(v)} \Delta_k P(\boldsymbol{X}) \; A_k(\boldsymbol{X}) \boldsymbol{n}_k(\boldsymbol{X}) + \sum_{k \in f(v)} E_k \varepsilon_k^e(\boldsymbol{X}) a_k(\boldsymbol{X}) \boldsymbol{e}_{k,v}(\boldsymbol{X}),$$

  where F_k^n is the k-th component of $\boldsymbol{F}^n$, and with the same notations as in Eq. 11 from main text; $\boldsymbol{P}(\boldsymbol{X})$ and $\boldsymbol{\varepsilon}(\boldsymbol{X})$ are the functions of $\boldsymbol{X}$ given by Eq. (S27) and Eq. (S28). Then, the new position of the vertices $\boldsymbol{X}^{n+1}$ is the solution of the equation

$$\boldsymbol{F}^n(\boldsymbol{X}) = 0. \quad \text{[S29]}$$

Resolution of Eq. (S29)**.** This is the last and most critical step of the resolution algorithm. The problem of computing the roots of a multidimensional non linear function is often encountered in the mechanical modelling of complex multibody systems, and a method of choice for the resolution is the Newton algorithm [1]. It is a iterative process which derives from a Taylor expansion about a current point $\boldsymbol{u}^k$:

$$\boldsymbol{F}^n(\boldsymbol{u}^{k+1}) = \boldsymbol{F}^n(\boldsymbol{u}^k) + J(\boldsymbol{u}^k)(\boldsymbol{u}^{k+1} - \boldsymbol{u}^k) + o(\boldsymbol{u}^{k+1} - \boldsymbol{u}^k),$$

where $J(\boldsymbol{u}^k)$ is the jacobian matrix of function $\boldsymbol{F}^n$. The new value $\boldsymbol{u}^{k+1}$ is obtained by setting the right-hand side to zero and neglecting the high order term, and then solving the linear system:

$$J(\boldsymbol{u}^k)\delta\boldsymbol{u}^k = -F^n(\boldsymbol{u}^k), \boldsymbol{u}^{k+1} = \boldsymbol{u}^k + \delta\boldsymbol{u}^k.$$

With the initial value $\boldsymbol{u}^0 = \boldsymbol{X}^n$, iterations are run until a stopping criterium is met, for instance

$$\frac{\|\boldsymbol{F}^n(\boldsymbol{u}^k)\|}{\|\boldsymbol{F}^n(\boldsymbol{u}^0)\|} \leq tol_{res}, \quad \text{[S30]}$$

where $tol_{res} > 0$ is a fixed value. Then one can set $\boldsymbol{X}^{n+1} = \boldsymbol{u}^k$.

The compution of the jacobian matrix $J(\boldsymbol{u}^k)$ is non trivial here because of the numerous non-linearities of function $\boldsymbol{F}^n$. Therefore we have chosen to use the Newton-Krylov variant of this algorithm, that avoids the computation of the jacobian without loosing efficiency [1].

However, Newton methods in general have only local convergence properties, which means that they need an initial guess close enough to the solution to be able to converge. This is critical for instance in the first time step of the simulation, because the initial conditions might be far from equilibrium, but also for further time steps. This lack of global convergence properties is often dealt with by adding a friction term proportional to the velocity and hence to the time derivative of the positions. With this method, the problem to solve at each time step becomes after time discretization: find $\boldsymbol{X}$ such that

$$\boldsymbol{G}(\boldsymbol{X}) = \boldsymbol{F}^n(\boldsymbol{X}) - c\frac{\boldsymbol{X} - \boldsymbol{X}^n}{\Delta t} = 0,$$

where $c > 0$ is a friction coefficient. This new problem is easier to solve with the Newton method, all the more that c is large. However, the root of $\boldsymbol{G}$ might not satisfy the condition Eq. (S30), and in addition its value depends on the value of c. Therefore, instead of applying the Newton method to the function $\boldsymbol{G}$, we perform the following iterative process:

- Initialization: $\boldsymbol{u}^0 = \boldsymbol{X}^n$
- Assuming $\boldsymbol{u}^k$ is known, compute $\boldsymbol{u}^{k+1}$ as the solution of

$$\boldsymbol{G}^k(\boldsymbol{u}^{k+1}) = 0, \qquad \text{[S31]}$$

  where $\boldsymbol{G}^k(\boldsymbol{u}^{k+1}) = \boldsymbol{F}^n(\boldsymbol{u}^{k+1}) - c^k\frac{\boldsymbol{u}^{k+1}-\boldsymbol{u}^k}{\Delta t}$, and the value $c^k > 0$ will be adjusted to ensure a robust convergence (see below). This solution is computed thanks to the Newton method, with the tolerance $tol_{res}/10$ in the stopping criterium.
- The iterations are stopped when $\frac{\|\boldsymbol{F}^n(\boldsymbol{u}^k)\|}{\|\boldsymbol{F}^n(\boldsymbol{u}^0)\|} \leq tol_{res}$. Then the choice $\boldsymbol{X}^{n+1} = \boldsymbol{u}^k$ is an approximate solution of Eq. (S29).

In this algorithm, the choice of the friction coefficient c^k is not straightforward: a large value would ensure the convergence of subproblem Eq. (S31), but it would also slow down the convergence toward the solution of problem Eq. (S29). To avoid this, we choose a large initial value c^0 and decrease it with the law $c^{k+1} = c^k/2$. This choice ensures a robust behaviour of the algorithm.

3. Sets of parameters used for the bump simulations

Let $R_0 = 10\mu$m be the initial radius of the cell, then $P^Y = \frac{w}{R_0\cos(\pi/6)}E\varepsilon^Y$ is a representative value for the yield turgor of a hexagonal cell. However we have observed that the effective threshold pressure is approximately twice lower in multicellular tissues and we have adapted the value of E accordingly: we choose E such that $P^Y = 0.5$ MPa and multiplied this value by two to obtain a an order of magnitude for the initial turgor of the cell close to the target value 0.5 MPa. The value $\varepsilon^Y = 0.1$ is chosen accordingly to experimental observations where wall deformations can be of the order of 10%. We choose two values for P^M: 0.55 MPa close to the threshold, and 0.7 MPa. Finally, we can use the Lockhart's prediction $\dot{\gamma}^*$ (Eq.6 from main text) as an order of magnitude of the relative growth rate; we choose $\dot{\gamma}^* = 2\% \cdot \mathrm{h}^{-1}$. Then, a given value of α^a (evaluated with $R = R_0$) sets a unique value of L^a and ϕ^w. The table S1 recapitulates the sets of parameters used in this article, either with the control parameters

$$\varepsilon^Y, P^M, P^Y, \dot{\gamma}^*, \alpha^a, \qquad \text{[S32]}$$

or equivalently with the actual parameters of the model

$$\varepsilon^Y, P^M, E, \Phi^w, L^a. \qquad \text{[S33]}$$

The correspondance has been obtained with $R_0 = 6.5\mu$m.

References

1. Knoll DA, Keyes DE (2004) Jacobian-free newton-krylov methods: a survey of approaches and applications. *J Comp Phys* 193:357–397.

Table S1. Parameters used for the bump simulation (see Fig. 3 in main text). The top part of the table refers to the control parameters Eq. (S32)**, and the bottom part to the actual parameters** Eq. (S32) **used in the 2D model. The rightmost parameters after the vertical double bar are specific to multicellular models as they quantify the water conductivity between neighbour cells. The geometrical parameters are** $h = 10\mu\text{m}$ **and** $w = h/20$**.**

Control parameters	ε^Y	P^M (MPa)	P_6^Y (MPa)	$\dot{\gamma}^*$ (h^{-1})	α^a	α^s
(REF)	0.1	0.7	0.5	$2 \cdot 10^{-2}$	0.1	0.9
(CC-)	0.1	0.7	0.5	$2 \cdot 10^{-2}$	0.1	0.1
(ALPHA+)	0.1	0.7	0.5	$2 \cdot 10^{-2}$	0.9	0.9
(PM-)	0.1	0.55	0.5	$0.5 \cdot 10^{-2}$	0.1	0.9
Actual parameters	ε^Y	P^M (MPa)	E (MPa)	Φ^w ($\text{MPa}^{-1}.\text{s}^{-1}$)	L^a ($\text{m.MPa}^{-1}.\text{s}^{-1}$)	L^s ($\text{m.MPa}^{-1}.\text{s}^{-1}$)
(REF)	0.1	0.7	112.6	$2.8 \cdot 10^{-5}$	$8.7 \cdot 10^{-11}$	$7.8 \cdot 10^{-10}$
(CC-)	0.1	0.7	112.6	$2.8 \cdot 10^{-5}$	$8.7 \cdot 10^{-11}$	$9.6 \cdot 10^{-12}$
(ALPHA+)	0.1	0.7	112.6	$3.1 \cdot 10^{-6}$	$7.8 \cdot 10^{-10}$	$7.0 \cdot 10^{-9}$
(PM-)	0.1	0.55	112.6	$2.8 \cdot 10^{-5}$	$8.7 \cdot 10^{-11}$	$7.8 \cdot 10^{-10}$